



On hydrodynamic and electrical characteristics of a self-powered triboelectric nanogenerator based buoy under water ripples

Yunpeng Zhao^{a,c,*}, Zhongqi Fan^a, Chunwei Bi^a, Hao Wang^b, Jianchun Mi^d, Minyi Xu^{b,*}

^a State Key Laboratory of Coastal and Offshore Engineering, Dalian University of Technology, Dalian 116024, China

^b Dalian Key Lab of Marine Micro/Nano Energy and Self-powered Systems, Marine Engineering College, Dalian Maritime University, Dalian 116026, China

^c Ningbo Institute of Dalian University of Technology, Ningbo 315016, China

^d College of Engineering, Peking University, Beijing 100871, China

HIGHLIGHTS

- A self-powered triboelectric nanogenerator based buoy's numerical model is proposed.
- The buoy's hydrodynamic and electrical performance in small-amplitude waves is analyzed.
- A two-point mooring system of chains vertically to the wave ray favors the buoy application.
- The buoy has potential applications for powering marine internet of things.

ARTICLE INFO

Keywords:

Triboelectric nanogenerator
Wave energy extraction
Boundary element method
Power take-off damping
Electrical performance

ABSTRACT

Due to the bottom effect and the shading effect of the land, the energy density of the wave propagation to the coast reduces significantly, so that small-amplitude waves are widespread offshore. Triboelectric nanogenerators (TENGs) offer the prospect of obtaining the energy of small-amplitude waves with centimeter-level wave heights offshore. This study proposes a numerical model of a self-powered sandwich-like TENGs (S-TENGs) based buoy. The model is calibrated and verified through experiments. The effects of various parameters (e.g., mooring configuration, wave frequency, and wave height) on the hydrodynamic and electrical performance of the buoy under small-amplitude waves of centimeter-level wave height are analyzed. We demonstrated that it is more conducive for the device to extract wave energy when the mooring lines are perpendicular to the wave direction. The device's peak power is 61.20 mW when the wave height is 6 cm, and the wave frequency is the natural frequency of the device. Moreover, the angle between the S-TENG electrodes and wave direction varies slightly varied near the buoy's natural frequency, thus, affecting the electrical properties of the device. At the same time, the electrical performance is sensitive to the incident wave height. This study provides a reference on the benefits of TENGs based self-powered buoys applications for powering marine sensing facilities, marine ranches, and lake environmental monitoring.

1. Introduction

Due to the limited amount of traditional fossil energy and the strengthening greenhouse effect, the development of renewable and clean energy has become a common goal worldwide [1]. Marine renewable energy has promising prospects compared with traditional renewable energy, as wave energy features the advantages of cleanliness, renewability, high energy density, and attracts extensive attention

[2]. At present, the extraction of wave energy is mainly performed by electromagnetic generators (EMGs), which face the disadvantages of heavy mass, high cost, and easy corrosion [3]. At the same time, the existing large-scale wave energy converters (WEC) for wave energy extraction by EMGs require sufficiently high energy density. Thus, most of them are placed in the open ocean, with few hundred kilometers away from coasts. As the wave travels to the shore, the wave energy is significantly decreased attribute to bottom effects (such as wave

* Corresponding authors at: State Key Laboratory of Coastal and Offshore Engineering, Dalian University of Technology, Dalian 116024, China (Y. Zhao). Dalian Key Lab of Marine Micro/Nano Energy and Self-powered Systems, Marine Engineering College, Dalian Maritime University, Dalian 116026, China (M. Xu).

E-mail addresses: ypzhao@dlut.edu.cn (Y. Zhao), xuminyi@dlmu.edu.cn (M. Xu).

<https://doi.org/10.1016/j.apenergy.2021.118323>

Received 5 October 2021; Received in revised form 28 November 2021; Accepted 1 December 2021

0306-2619/© 2021 Published by Elsevier Ltd.

refraction, diffraction, underwater friction, and wave breaking) and the complex effects of shading due to the presence of land (such as islands and headlands) [4]. Therefore, unlike large waves several meters high in the open ocean, small-amplitude waves within centimeters high are more common in offshore areas. Lavidas et al. [5], Choupin et al. [6], Kamranzad and Hadadpour [7] used the wave height of 0.5 m as the cut-in and the wave height of 4 m as the cut-off to classify the sea area where WECs are located into low, intermediate and high energy density areas. Therefore, the sea areas with centimeters-level wave height can be considered as low energy density sea areas. For these low energy density sea areas, wave energy extraction by large-volume WECs based on EMGs is no longer applicable. Hence, it is essential to develop more appropriate technologies for extracting wave energy from the small-amplitude waves.

In 2012, Wang et al. [8] proposed the triboelectric nanogenerator (TENG) concept, which can efficiently extract energy from various sources, such as sound, wind, ocean current, low-frequency wave, etc [9–12]. Meanwhile, they can be combined with high precision sensing facilities [13]. In contrast to EMGs, TENGs provide higher energy output performance in low-frequency environments and the advantages of flexibility, portability, and economy [14]. Thus, the extraction of wave energy using TENGs should have a broad prospect [15]. Different forms of TENGs have been designed for the extraction of wave energy. For instance, Zhang et al. [16] designed a sea snake structure wave energy converter based on TENGs, but the device can only collect wave energy in a specific direction. Xu et al. [17] proposed a tower-like TENG capable of harvesting arbitrary directional wave energy, but the output performance of multiple parallel-connected units needs to be further investigated. Zhang et al. [18] presented a self-powered intelligent buoy system (SIBS) powered by a multilayered TENG. However, the electrical characteristics of the device have to be further optimized. In our previous works, Wang et al. [19] investigated the power output performance of a sandwich-like triboelectric nanogenerators (S-TENGs) through a series of physical modeling experiments. It has been demonstrated that a new type of self-powered buoy with pitching motion formed by seven S-TENG units in parallel could effectively extract wave energy under wave action. However, this work focused only on the structural design and primary output performance of the S-TENG. A systematic study of the hydrodynamic characteristics of the self-powered buoy has not been conducted.

This study proposes a numerical model based on S-TENGs self-powered buoy, which is calibrated and validated by experiments. Numerical simulations and experiments are performed to investigate the hydrodynamic and electrical characteristics of the self-powered buoy under the small-amplitude waves within centimeters high. This study also provides a reference for applying self-powered buoys in the power supply of offshore sensing facilities, marine ranches, lake environment monitoring.

The structure of this study is as follows. Section 2 briefly describes the physical model tests and numerical simulation method used, and the numerical model is calibrated and validated. Section 3 presents the systematic analysis of the hydrodynamic and electrical characteristics of S-TENGs based self-powered buoy for different wave heights, wave frequencies, and mooring configurations. Finally, the conclusions are presented in Section 4.

2. Methods

2.1. Experimental method

While investigating the self-powered buoy under small-amplitude waves of centimeter-scale wave heights, it is crucial to analyze the device's hydrodynamic and electrical characteristics, and to identify the various factors affecting its energy conversion. Therefore, it is necessary to conduct a systematic experimental study under regular waves [20].

The experiments of this study were conducted in a wave-current tank

for the marine environment at the State Key Laboratory of Coastal and Offshore Engineering, Dalian University of Technology, China. The flume dimensions are 50 m in length, 3 m in width, and 1 m in depth. Waves are generated with a piston-type unidirectional wavemaker installed at one end of the tank. A wave-absorbing beach is located at the other end to reduce the wave reflection.

Fig. 1(a) schematically shows the experimental setup. The self-powered buoy was arranged 25 m away from the wavemaker and 1.5 m away from the sidewall of the water tank. Bachynski et al. [21] concluded that a slack mooring system only affects the pitch motion of WEC at a shallow frequency. Therefore, two steel rings were attached to the bottom of the buoy at 0.05 m on both sides of the axis, which along the incident direction of the wave, and were connected to the bottom of the tank by 1.05 m long stainless-steel slack anchor chains to reduce the adverse effect of the mooring system pretension on the pitch motion of the device. The diameter of the anchor chains is 5 mm, the mass per unit length is 0.09 kg/m, the axial stiffness is 1232.76 kN/m³, and the maximum bearing capacity is 88.2 kN. During the experiments, six capacitive wave gauges were arranged upstream and downstream of the self-powered buoy to measure the surface elevations, as shown in Fig. 1(b). The absolute accuracy of those gauges is ± 1 mm. The sampling frequency was set to 100 Hz during the measurements, and the stable data of 20.48 s was selected for data analysis. The motion response of the buoy was tracked through a high-speed CCD camera recorded from three light-emitting diodes, which had been fixed on the top of the outer pontoon (see Fig. 1(c)). Then the captured video was transformed into visualized data of the response through the data processing software system. The high-speed CCD camera has an absolute accuracy of ± 1 mm in displacement and $\pm 10^{-3}^\circ$ in angle.

Due to the flexibility and lightweight of TENG, the prototype can be used to test directly in the test process, thereby reducing the complexity of the power take-off (PTO) system simulation caused by the Froude scaling. The self-powered buoy consists of an external buoy, a PTO system composed of the seven S-TENG units in parallel, and a counterweight unit (see Fig. 1(d)). The external buoy is made of acrylic, with a diameter of 0.35 m and a height of 0.4 m, which isolates the internal unit from the external environment, thus reducing the impact of humidity on the power generation efficiency of the S-TENG units. Each internal S-TENG unit is a cylindrical structure with a diameter of 0.1 m and a height of 0.2 m (see Fig. 1(e)), and it contains ten layers of internal structure (Fig. 1(f)). Each layer of the structure contains an acrylic frame, aluminum electrode, and polytetrafluoroethylene (PTFE) balls, and all electrode directions in the device are consistent. Under the wave excitations, the self-powered buoy produces pitch motion, which makes the PTFE balls in S-TENG units roll back and forth on the aluminum electrodes. After repeat friction with the electrodes, the balls are negatively charged. When the PTFE balls contact one electrode, the electrode is positively charged. With the balls moving back, they contact another electrode to make it positively charged, thus forming a current in the circuit. More detailed descriptions can be found in Ref. [19]. In this study, the buoy's short-circuit current I_{SC} and transfer charge Q_{SC} were measured by a Keithley 6514 system electrometer. The Keithley 6514 system electrometer absolute accuracy of ± 1 fA in current and 10 fC in charge.

Fig. 2(a) defines the angle α between the direction of wave and electrodes. As α varies, I_{SC} and Q_{SC} generated by the S-TENG change significantly, as shown in Fig. 2(b, c), respectively. When $\alpha = 90^\circ$, I_{SC} and Q_{SC} reach their peak values, and the power generation efficiency is highest. Therefore, the wave direction and the electrode direction should be perpendicular to each other during the test. Due to the single point mooring system (Fig. 2(d)), the buoy produces a yaw motion around the z-axis under the wave action, thus, affecting the stability of the device's electrical output performance, as shown in Fig. 2(e, f). During the test, a two-point mooring system was chosen to constrain the angle α . In order to determine the effect of the mooring configuration of

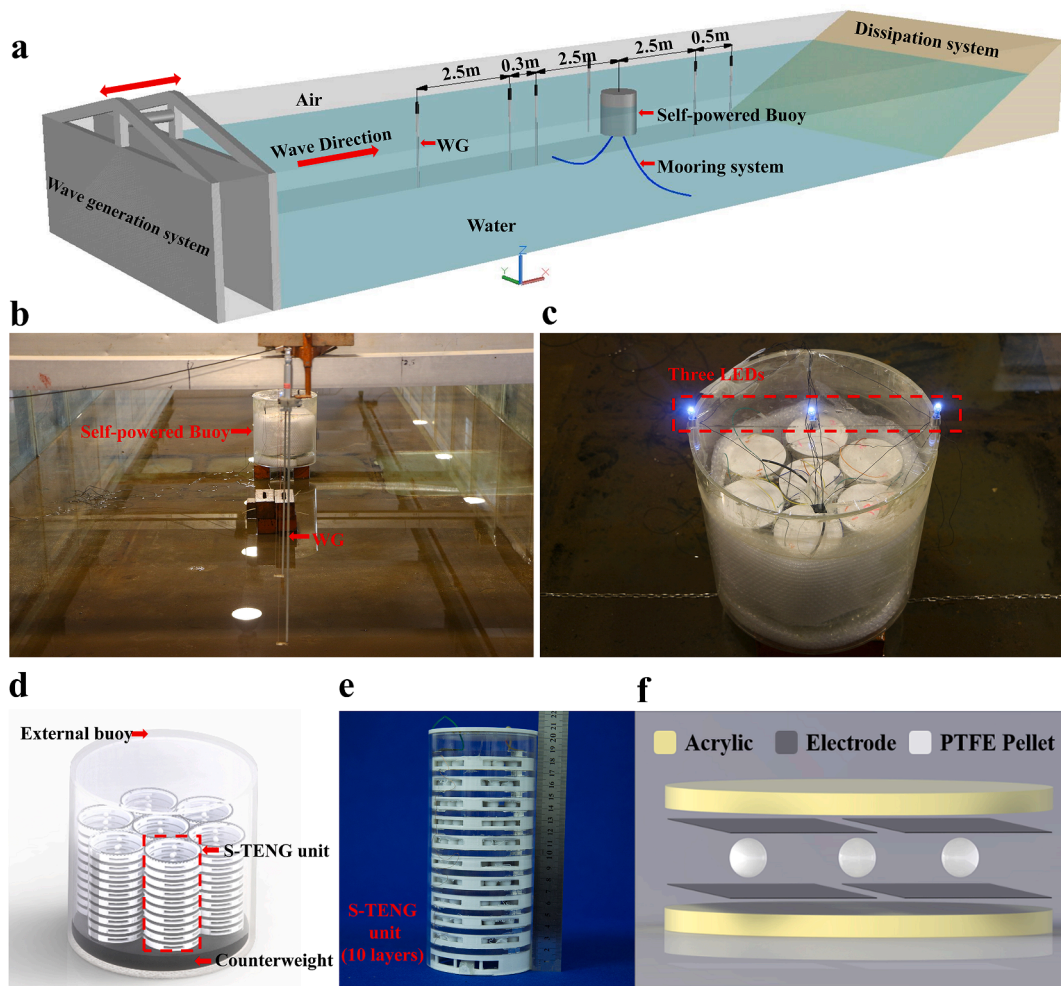


Fig. 1. Experiment layout and the structure of the self-powered buoy. (a) 3D schematic of the experiment setup; (b) physical scene in the wave-current tank; (c) three light-emitting diodes fixed to on the top of the self-powered buoy; (d) schematic diagram of the self-powered buoy; (e) physical diagram for the S-TENG unit containing ten layers of internal structure; (f) schematic diagram for each layer of the S-TENG unit.

the self-powered buoy on the device's energy conversion, two two-point mooring methods were chosen. The mooring lines are set perpendicular to the wave ray named mooring configuration I (MC I) and parallel to the wave ray named mooring configuration II (MC II) for comparative tests, as shown in the scheme of Fig. 2(g, h).

During the whole test process, the water depth h and the self-powered buoy draft d remain constant ($h = 0.7$ m and $d = 0.28$ m). The weight and proportion of each part of the device are listed in Table 1. In order to study the hydrodynamic and electrical characteristics of the device under the centimeter-level small-amplitude waves, the wave height was set at 4 cm and 6 cm (where the wave height of 4 cm is the smallest amplitude wave that the wavemaker can generate). The specific wave parameters are listed in Tables 2 and 3, respectively. The experimental data were measured three times to ensure the required accuracy, and the average values were obtained to reduce the impact of systematic errors.

2.2. Numerical simulation

Due to the long test period of the physical model, which focuses on analyzing specific conditions, numerical simulations can be used for analyzing the effects of different factors on the wave energy conversion of self-powered buoys over a broader range of wave frequencies. The methods to study WECs' hydrodynamic properties in waves primarily include potential flow theory and computational fluid dynamics (CFD).

The latter can study practical nonlinear factors, such as fluid viscosity, but requires more computational resources. The potential flow theory enables to study of the nonlinear factors with some modification while ensuring computational efficiency, such as adding a damping term to account for the fluid viscosity. Most of the wave conditions' wave steepness is much less than 1 in this study, and the wave nonlinearity can be neglected. Therefore, the potential flow theory was chosen to study the hydrodynamic characteristics of S-TENGs based self-powered buoy in linear waves. Numerical simulations of the S-TENGs based self-powered buoy were conducted by ANSYS AQWA [22].

2.2.1. Numerical model

The numerical model based on the boundary element method was proposed to simulate the hydrodynamic properties of the self-powered buoy. The numerical model of the self-powered buoy was simulated using surface elements. Fig. 3(a) shows the schematic of the numerical model and the grids of the buoy.

The self-powered buoy's kinematic equation in the frequency domain can be expressed below [23]:

$$-\omega^2 \{ [M] + [\mu] \} \{x\} - i\omega [B_{tot}] \{x\} + [K] \{x\} = \{f\} \quad (1)$$

where $[M]$ is the device's mass matrix, $[\mu]$ is the additional mass matrix of the structure; $[B_{tot}] = [B] + [B_{vis}] + [B_{pro}]$ is the total damping matrix, $[B]$ is the radiation damping matrix, which is relevant to the wave form energy dissipation, $[B_{vis}]$ is the viscous damping matrix, which accounts for the

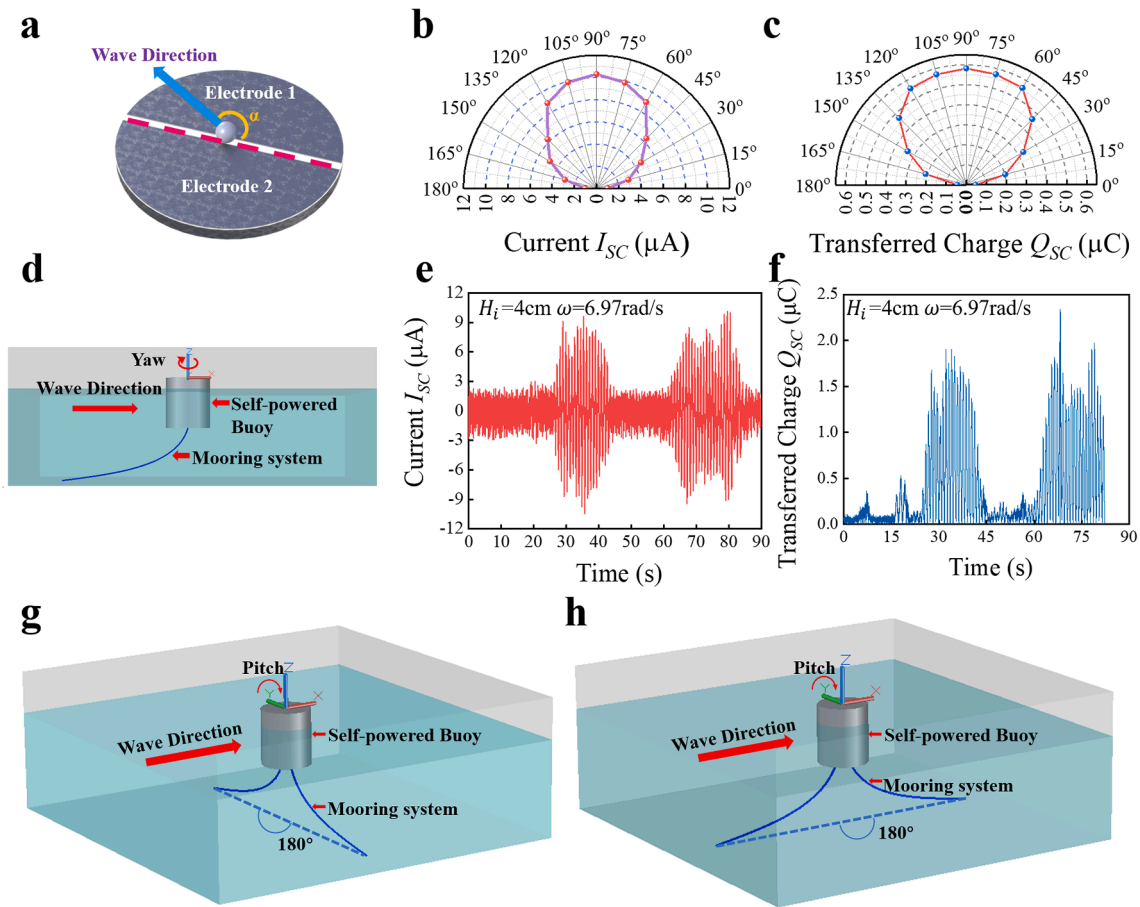


Fig. 2. Electrical characteristics of the S-TENG unit under the wave action in different directions and schematic diagrams of different mooring configurations employed by the self-powered buoy. (a) Defining the angle α between the wave direction and electrode direction; (b) directional map of the short-circuit current I_{SC} ; (c) directional map of the transfer charge Q_{SC} ; (d) schematic of the self-powered buoy with single point mooring; (e, f) time histories of I_{SC} and Q_{SC} of the self-powered buoy under single point mooring condition; (g) mooring lines perpendicular to the wave ray (mooring configuration I); (h) mooring lines parallel to the wave ray (mooring configuration II).

Table 1

The parameters of each component of the self-powered buoy.

| Component | Mass (kg) | specific weight (%) |
|------------------|-----------|---------------------|
| PTFE balls | 1.36 | 4.89 |
| Frame of S-TENGs | 5.22 | 18.78 |
| External Buoy | 3.72 | 13.38 |
| Clump Weight | 17.5 | 62.95 |

Table 2

Wave conditions of the validation tests.

| H_i (cm) | T (s) | ω/ω_n |
|------------|--|--|
| 6 | 0.66, 0.75, 0.87, 1.03, 1.04, 1.05, 1.20, 1.30, 1.46, 1.62, 1.72, 1.88 | 1.60, 1.40, 1.20, 1.01, 1.00, 0.99, 0.87, 0.80, 0.71, 0.64, 0.60, 0.55 |

H_i is the incident wave height, T denotes the wave period, ω is the wave frequency, and ω_n denotes the natural frequency of the self-powered buoy.

Table 3

Wave conditions of the formal tests.

| H_i (cm) | T (s) | ω/ω_n |
|------------|-------------------------------------|----------------------------------|
| 4 | 0.66, 0.75, 0.87, 1.03, 1.04, 1.05, | 1.60, 1.40, 1.20, 1.01, 1, 0.99, |
| 6 | 1.30 | 0.80 |

fluid viscosity effect. The effect of fluid viscosity can be decomposed into three parts: inertia due to water acceleration, the effect due to viscous boundary layer, and the effect due to vortex shedding [24]. $[B_{PTO}]$ is the PTO damping matrix, which represents the effect of the TENG units within the buoy; $[K]$ is the stiffness matrix of the system, including the linear hydrostatic stiffness and additional stiffness of the anchor chains; $\{x\}$ is the displacement amplitude matrix of the structure, $\{f\}$ is the 6×1 matrix of all combinations of external forces as function of wave frequency ω .

As shown in Table 1, the PTFE balls' mass is less than 5% of the total mass of the self-powered buoy. Thus, the effect of the relative motion between the balls and the buoy on the device's inertial moment is neglected in the modeling process. The balls' mass is equated to the structure. As displayed in Fig. 2(g), the buoy generates pitch motion around the y-axis under waves, which drives the movement of the internal PTFE balls, resulting in the PTO damping. In the present study, a linear damping model simulated the PTO damping according to the mechanical features of the balls' motion in the experimental model [17].

The PTO resistance for the self-powered buoy's pitch direction can be expressed as:

$$F_{PTO} = B_{PTO,ry} \cdot \omega RY \quad (2)$$

where ω is the wave frequency, $B_{PTO,ry}$ is the PTO damping of the S-TENG units in pitch motion, and RY is the pitch motion amplitude of the self-powered buoy in the frequency domain. The pitch response amplitude operator (RAO) is the ratio between RY and the incident wave amplitude

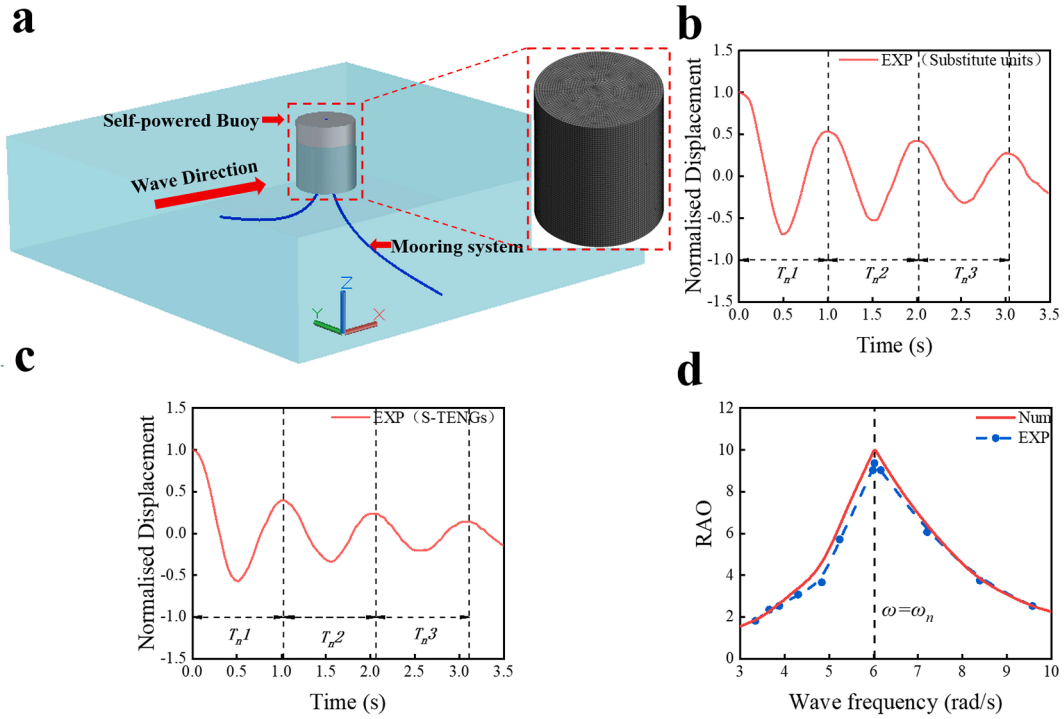


Fig. 3. The present numerical model of the self-powered buoy and its calibration and validation. (a) Numerical model of the moored self-powered buoy and meshing of the numerical model; (b) motion time series of the device with substitution units; (c) motion time series of the device with S-TENG units; (d) comparison of the experimental results with numerical simulations for the self-powered buoy pitch response amplitude operator (RAO) with MC I.

or the half wave height ($H_i/2$), i.e.,

$$RAO = \frac{RY}{H_i/2} \quad (3)$$

The average power absorbed by the PTO system from the incident wave can be obtained below:

$$P_{abs} = \frac{1}{2} \omega^2 B_{PTO,ry} RY^2 \quad (4)$$

The capture width ratio (CWR) of the device can be expressed as:

$$\eta = \frac{P_{abs}}{P_{in} \cdot D} \quad (5)$$

where D is the device's diameter and P_{in} is the average power of the incident wave, which represents the work done by the dynamic pressure on the fluid in one wave period, i.e.,

$$P_{in} = \frac{1}{16} \frac{\omega \rho g H_i^2}{k} \left(1 + \frac{2kh}{\sinh(2kh)} \right) \quad (6)$$

where ρ is the water density, g is the acceleration of gravity, h is the water depth, and k is the wave number.

2.2.2. Calibration and validation of the numerical model

In order to calibrate and verify the numerical model of the self-powered buoy, which is used to simulate the PTO system with a linear damping model, two types of tests were performed.

Firstly, the free decay tests were performed to determine the natural frequency and PTO damping coefficient of the self-powered buoy. The device without a mooring system was placed in the center of the water tank for the free decay test. Because there are many PTFE balls in S-TENG units, contact collision and other complex phenomena occur between the balls during the movement of the device. The free decay test was carried out with the same shape and mass substitutable units as the S-TENG units, and then the S-TENG units were put into the buoy to carry out the free decay test under identical test conditions.

In still water, after releasing from the initial position, the device's motion decays until it returns to the equilibrium position. The corresponding motion equation in the time domain is as follows [23]:

$$ry(t) = ry_0 \sqrt{1 + \left(\frac{\gamma}{\omega_n} \right)^2} e^{-\gamma t} \cos \left(\omega_n t - \arctan \frac{\gamma}{\omega_n} \right) \quad (7)$$

where $ry(t)$ is the pitch angle in the time domain while ry_0 is the initial value; $\gamma = B_{tot}/[2(M+\mu)]$ is the decay factor; $\omega_n = \sqrt{\omega_d^2 - \gamma^2}$ and $\omega_d = \sqrt{K/(M+\mu)}$ are the damped and undamped natural frequencies, respectively. Here, K is the hydrostatic restoring force coefficient, M is the moment of inertia and μ is the added mass moment of inertia.

The initial pitch angle of the self-powered buoy in the free decay tests was 0.227 rad. The tests were repeated three times to eliminate random and systematic errors. A representative group of test results was selected for normalization, and the displacement time series with substitution units and S-TENG units were obtained, as shown in Fig. 3(b, c), respectively. Correspondingly, the resonance period and the logarithmic decrements of the device can be measured. The detailed data are presented in Tables 4 and 5. Based on the above results, the resonance period of the self-powered buoy is $T_n = 1.04$ s, which agrees well with the result calculated by the potential flow theory. The natural frequency of the device was measured to be $\omega_n = 6.02$ rad/s, whereas the PTO damping coefficient was $B_{PTO} = 0.276$ N·m/(rad/s).

Secondly, the absence of waves in the free decay experiment may lead to highly conservative damping forces [25], which plagues the

Table 4

The resonance period T_n of the self-powered buoy, according to Fig. 3(b, c).

| | T_{n1} (s) | T_{n2} (s) | T_{n3} (s) | \bar{T}_n (s) |
|--------------------|--------------|--------------|--------------|-----------------|
| Substitution Units | 1.00 | 1.02 | 1.02 | 1.01 |
| S-TENG Units | 1.02 | 1.05 | 1.04 | 1.04 |

\bar{T}_n is the average resonance period of the device.

Table 5

The logarithmic decrements of the self-powered buoy according to Fig. 3(b, c).

| | $\ln(ry_0/ry_1)$ | $\ln(ry_1/ry_2)$ | $\ln(ry_2/ry_3)$ |
|--------------------|------------------|------------------|------------------|
| Substitution Units | 0.61 | 0.26 | 0.45 |
| S-TENG Units | 0.93 | 0.52 | 0.53 |

calibration of the model's damping coefficients. In order to verify the numerical model, free motion tests were conducted. Fig. 3(d) shows the comparison of the numerical simulations with experimental measurements for the self-powered buoy pitching RAO with MC I to validate the numerical model. The PTO damping was taken into account by adding linear damping in the numerical simulation process, and the corresponding structural parameters were consistent with those for the experimental tests. The wave conditions during the validation process are also identical for the experimental tests and numerical calculations. The specific parameters are listed in Table 2.

Evidently, the difference between the experimental and simulation results is overall very small, except near the natural frequency of the device at $0.87 < \omega/\omega_n < 1.20$, where the simulations exceed the experimental results. This distinction can be attributed to the unavoidable mechanical friction and the effect of fluid viscosity, which are nonlinearly increased with the pitch response amplitude of the device [26,27]. During the numerical simulation, the mechanical friction and fluid viscosity were simulated by a linear damping model. On the other hand, the effect of the PTFE balls colliding with each other caused by the buoy motion was neglected during the simulation. These may be the reasons for deviations between experiments and numerical calculations. Nevertheless, the experimental results and numerical simulation results generally agree well, proving the correctness of the numerical model.

The numerical model can calculate the hydrodynamic characteristics of the self-powered buoy, and the specific wave conditions for the numerical simulation are listed in Table 6.

3. Results and discussion

3.1. Hydrodynamics performance of S-TENGs based self-powered buoy

In this subsection, the effects of the mooring configuration, incident wave frequency (ω), and wave height (H_i) on the hydrodynamic performance of the self-powered buoy are analyzed.

First of all, let us investigate the effect of the two mooring configurations. For the wave height $H_i = 4$ cm, the specific values of the wave frequency ω are listed in Tables 3 and 6, respectively. The hydrodynamic characteristics and capture width ratio (CWR) of the self-powered buoy numerical and experimental results under different mooring configurations are demonstrated in Fig. 4.

Fig. 4(a) displays the experimental layout. Fig. 4(b, c) compare for the simulations and experiments the time histories of pitching responses with the mooring configurations MC I and II at $H_i = 4$ cm and $\omega = \omega_n$. Obviously, the experimental and numerical results agree very well with each other. Fig. 4(d) shows the amplitude spectra of the corresponding pitch response of the self-powered buoy with MC I from the simulations and experiments. First-order harmonics are used to calculate the device's RAO, and second-order harmonics are used to evaluate the nonlinear effects of the device. As shown in Fig. 4(d), the contribution of the second-order sum frequency component can be neglected at $H_i = 4$ cm and $\omega = \omega_n$.

Table 6

Wave conditions of the numerical calculation in formal test.

| H_i (cm) | T (s) | ω/ω_n |
|------------|-------------------------------------|-------------------------------------|
| 2 | 0.66, 0.70, 0.75, 0.80, 0.87, 0.95, | 1.60, 1.50, 1.40, 1.30, 1.20, 1.10, |
| 4 | 1.03, 1.04, 1.05, 1.16, 1.30, 1.49 | 1.01, 1.00, 0.99, 0.90, 0.80, 0.70 |
| 6 | | |

Fig. 4(e) illustrates the pitch RAO of the self-powered buoy versus different wave frequencies with the two mooring configurations. The peak frequencies of the pitch RAO of the device under the two different mooring methods are consistent. In particular, the pitch motion response of the device reaches its maximum as the wave frequency gradually approaches the natural pitching frequency of the self-powered buoy. It is worth noting that the wave frequency gradually approaches the natural frequency of the device at $0.87 < \omega/\omega_n < 1.20$, while the numerical results are slightly larger than the experimental ones. The nonlinear mechanical friction and fluid viscosity in the actual process are considered in the numerical method by a linear damping factor, which leads to overestimation. The pitching motion response of the device with MC I reaches the maximum value of $RY = 0.23$ rad at the resonant frequency, which exceeds the other mooring method by about 8%. This distinction is because MC II arranges the anchor chains parallel to the wave direction compared with MC I. The pitch motion amplitude of the self-powered buoy reaches its maximum at the resonance, and the anchor chain on the seaward side constrains the motion response of the device.

Fig. 4(f) demonstrates a difference in the CWR of the self-powered buoy (η) between the MC I and II. As the wave frequency (ω) gradually increases to ω_n , η reaches the maximum. As ω further rises, η will decrease. The linear damping model was used to approximate the fluid viscosity. This caused a slight overestimation of simulations compared with the experimental results, with a maximum relative error of about 5% for the case of $0.87 < \omega/\omega_n < 1.20$. It is worth noting that, at $\omega = \omega_n$, η takes its maximum value numerically of about 0.47 for MC I and 0.42 for MC II, versus the theoretical maximum value of 0.5 [28]. Namely, the use of MC I results in the CWR to be about 12% higher than that for MC II. It is more efficient for the self-powered buoy to extract wave energy by using MC I. Therefore, the device has good energy extraction characteristics under the small-amplitude wave of centimeters wave height. The MC I is used in the following research process.

Subsequently, the effect of the wave height (H_i) is studied, and the specific wave parameters are listed in Tables 3 and 6, respectively. The hydrodynamic characteristics and the capture width of the self-powered buoy with MC I for various H_i are shown in Fig. 5.

Because increasing the wave height significantly affects the wave nonlinearity, it is necessary to check the consistency between the experimental and numerical results. Fig. 5(a) shows the device's pitch motion response time series from the simulations and experiments for $H_i = 6$ cm and $\omega = \omega_n$. It can be seen that there is no significant deviation between the test and numerical results.

Fig. 5(b, c) displays the wave surface elevation around the self-propelled buoy for different H_i . As H_i increases, the wave surface elevation becomes more noticeable on the seaward side of the device. Fig. 5(d) shows the comparison of the amplitude spectra for the pitch response of the device between the simulations and experiments at various H_i for $\omega = \omega_n$. The influence of the second-order term can be ignored. It should be noted that there is noise in the experimental results compared to the calculated results for $H_i = 6$ cm. Due to the increase in H_i , the motion response for each degree of freedom of the device will increase, and the wave radiation will be more obvious. At the same time, the influence of reflected waves cannot be eliminated entirely in the wave tank, which leads to the diffraction, reflected, radiated, and incident waves are mixed to introduce noise.

Fig. 5(e) displays the pitch RAO versus the wave frequency for the self-powered buoy with different H_i . It can be seen that when $\omega = \omega_n$, as H_i increases from 2 cm to 4 cm, the device movement is small, the effect of fluid viscosity is not prominent. However, as H_i increases from 4 cm to 6 cm, the buoy's motion increases significantly, which generates more vortex shedding at the boundary of the structure and produces significant viscous dissipation [29]. At the same time, the effect of the nonlinear mechanical friction is more pronounced. According to the above analysis, with the increase of H_i , more energy dissipation is generated, which leads to the decrease in the pitch RAO of the device,

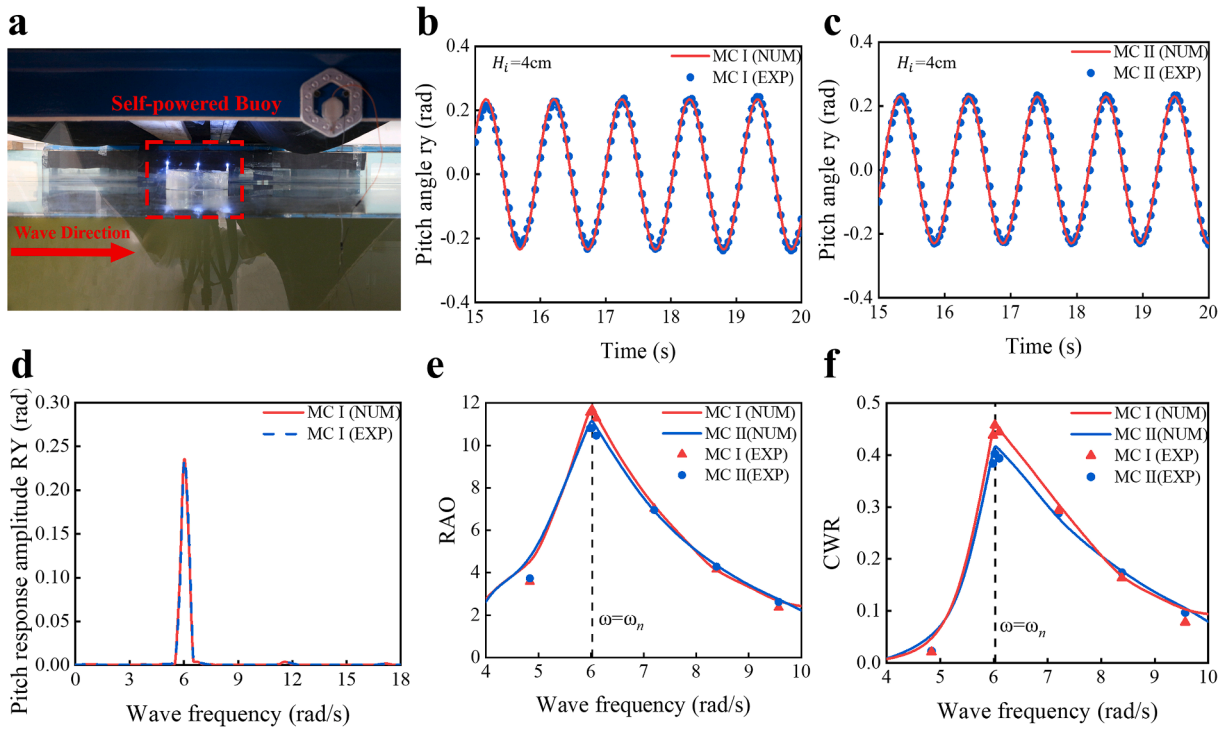


Fig. 4. Hydrodynamic characteristics and capture width ratio of self-powered buoys numerical and experimental results under MC I and II. (a) Experimental layout; (b, c) the buoy pitch response time histories for $H_i = 4$ cm and $\omega = \omega_n$; (d) amplitude spectra of pitch response with MC I when $H_i = 4$ cm and $\omega = \omega_n$; (e, f) the pitch RAO and capture width ratio (CWR) for MC I and II.

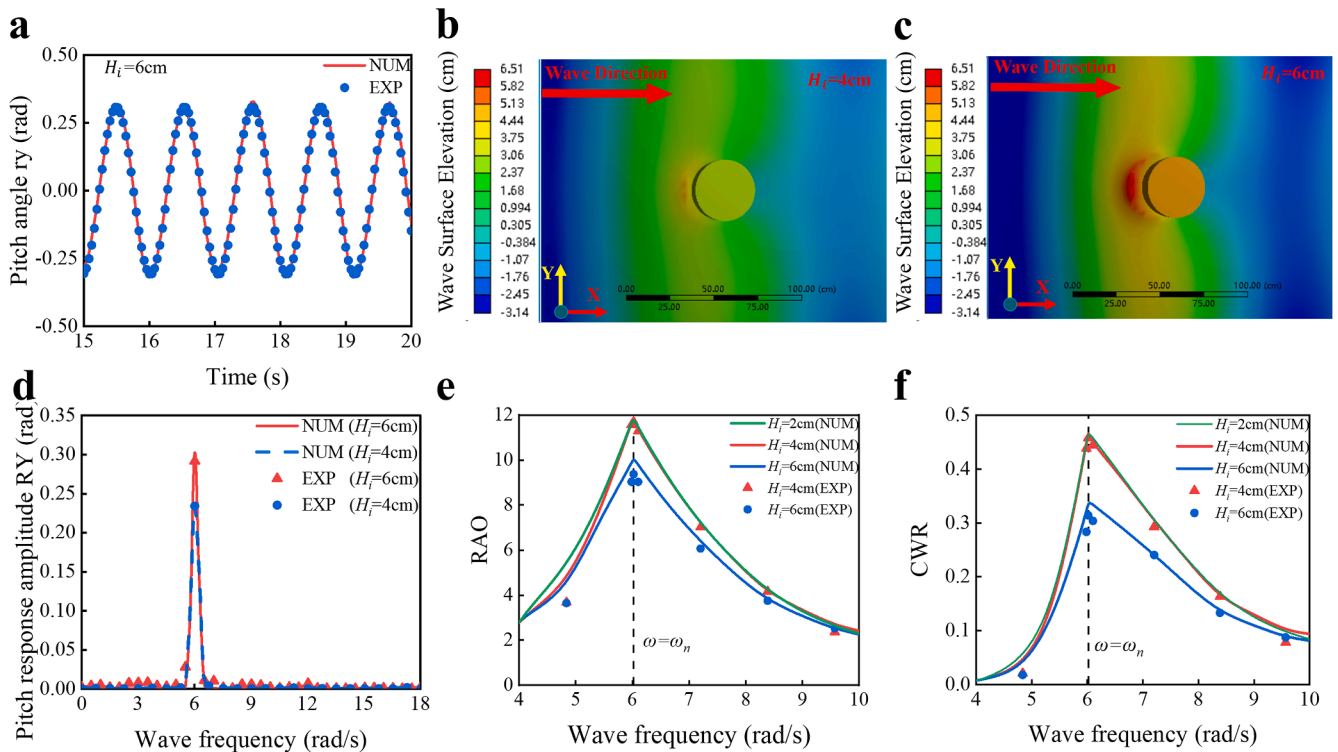


Fig. 5. Hydrodynamic characteristics and capture width ratio of self-powered buoy with MC I at different H_i . (a) Time histories of pitch response of the buoy between experimental and numerical results for $H_i = 6$ cm & $\omega = \omega_n$; (b, c) wave surface elevation around buoy at $H_i = 4$ cm & 6 cm for $\omega = \omega_n$; (d) pitch response amplitude spectra of the buoy at resonance. (e) pitch RAO and (f) CWR between experimental and numerical results.

and it is most apparent when $\omega = \omega_n$.

As shown in Fig. 5(f), when H_i increases from 2 cm to 4 cm, the effect of the fluid viscosity is not obvious. The CWR of the device almost no

decrease. However, as H_i increases from 4 cm to 6 cm, the wave frequency is near ω_n . The influence of fluid viscosity increases significantly with the increase of H_i , which leading energy loss and making the CWR

of the device decreases. When $H_i = 6$ cm, $\omega = \omega_n$, $\eta = 0.32$ accounting for approximately 68% of the CWR for $H_i = 4$ cm and $\omega = \omega_n$. It is worth noting that when $H_i = 6$ cm, the difference between the numerical and experimental results of the self-powered buoy's pitch RAO and CWR is greater than that when $H_i = 4$ cm (see Fig. 5(e, f)). The differences increment is caused by the experiment's noise effect when $H_i = 6$ cm (see Fig. 5(d)).

3.2. Electrical performance of S-TENGs based self-powered buoy

In this subsection, the electrical performance of the self-powered buoy is investigated. Simultaneously simulating the hydrodynamic and electrical properties of WECs is usually called the wave-to-wire modeling, which is widely used in wave energy research [30]. However, the wave-to-wire model is currently only applicable to electromagnetic generators. The numerical simulation method for TENGs' electric performance still in studying. Therefore, the numerical model proposed in this study was only used to simulate the hydrodynamic characteristics of S-TENGs based self-powered buoy, and the electrical performance of the buoy was studied by physical model tests. Since the minimum wave height that can be achieved in our laboratory is 4 cm in the wave frequency range of the test set. The case of $H_i = 2$ cm was not considered in the experimental process. The specific wave parameters are listed in Table 3.

Fig. 6 displays the electrical characteristics of the self-powered buoy with MC I for $H_i = 4$ cm and 6 cm. Fig. 6(a, b, c) respectively show the time series of the short-circuit current I_{SC} , the transfer charge Q_{SC} , and the open-circuit voltage V_{oc} of the self-powered buoy for different wave frequencies when $H_i = 6$ cm. In the relatively low-frequency region (0.80–1.00 ω_n), the motion response of the device increases with wave

frequency, which makes the device's power output parameters rise. The power output parameters reach their maxima at the device resonance point ($\omega = \omega_n$), especially $I_{SC} \approx 20.91 \hat{V}/A$, $Q_{SC} \approx 2.22 \hat{V}/C$, and $V_{oc} \approx 2.93$ kV, for $H_i = 6$ cm. When $\omega > \omega_n$, the power generation reduces significantly as ω rises since the power generation of S-TENG is affected more strongly by the motion amplitude.

Fig. 6(d, e) show the ω -dependent variation of the averaged short-circuit current \bar{I}_{SC} and transfer charge \bar{Q}_{SC} for the two cases of $H_i = 4$ cm and 6 cm. Both \bar{I}_{SC} and \bar{Q}_{SC} vary with ω similarly for different H_i . As expected, \bar{I}_{SC} and \bar{Q}_{SC} reach their peak values at $\omega = \omega_n$. Compared with the cases of $H_i = 4$ cm, the stability of the buoy electrical performance decreases at $H_i = 6$ cm. The decrease is explained by the fact that the device yaw motion amplitude around the z-axis increases with H_i , further changing α . As a result, the PTFE balls no longer move perpendicular to the gap between the two electrodes. Interestingly, \bar{Q}_{SC} just slightly changes as ω varies from ω_n to 1.2 ω_n . The reason is that, in both cases of $H_i = 4$ cm and 6 cm, the PTFE balls have been entirely driven to produce their maximum charges, which do not have a significant difference [19]. According to the single S-TENG unit's forced motion experiments, when the PTFE balls have been fully charged by the triboelectric effect, \bar{I}_{SC} of the unit still increases with the balls' motion amplitude increased at constant movement frequency, and it has a top roof [31]. Therefore, \bar{I}_{SC} of the S-TENG based self-powered buoy also has a maximum value when constant wave frequency.

Fig. 6(f) shows the device's power P_{elec} for $H_i = 4$ cm and 6 cm. Note that $P_{elec} = I_{SC,ext}^2 R$, where $I_{SC,ext}$ is the extremum of the short-circuit current, and R is the resistance of the seven S-TENG units ($R \approx 140$ M $\hat{\Omega}$). It is worth noting that the maximal values of P_{elec} occur at $\omega = \omega_n$, which are 61.20 mW and 46.72 mW for $H_i = 6$ cm and 4 cm,

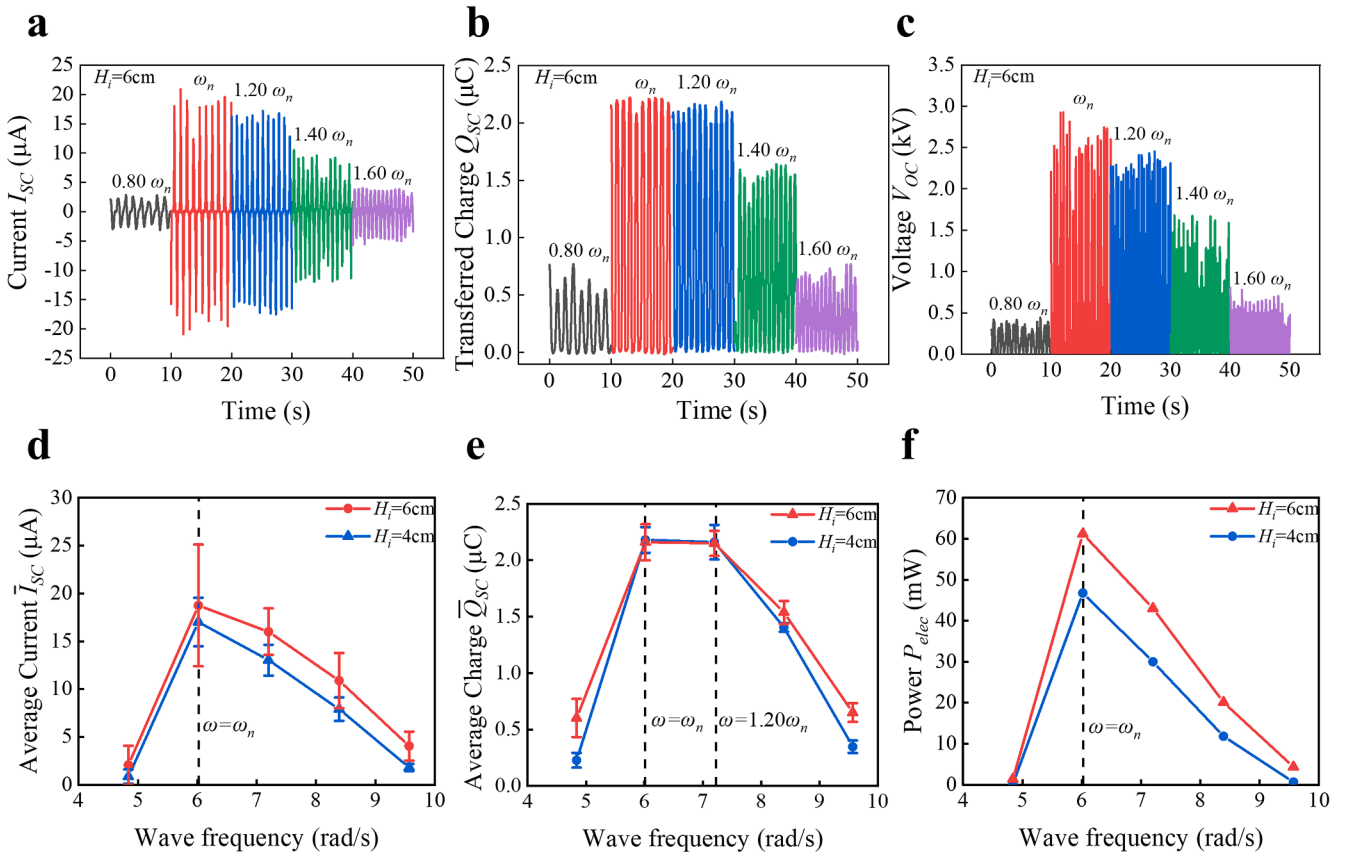


Fig. 6. Electrical characteristics with H_i when the self-powered buoy is moored in MC I. (a, b, c) Time histories of I_{SC} , Q_{SC} and V_{oc} with different wave frequencies when $H_i = 6$ cm; (d, e) averaged short-circuit current \bar{I}_{SC} and transfer charge \bar{Q}_{SC} versus wave frequency (ω) for $H_i = 4$ cm and 6 cm; (f) P_{elec} versus ω for $H_i = 4$ cm and 6 cm.

respectively. The former maximum is about 31% higher than the latter, while a 50% increase in H_i . This indicates a nonlinear increase in the maximal P_{elec} with an increase H_i . These nonlinear results are likely from several factors. For instance, as H_i increases, the effect of fluid viscosity becomes more significant, thus, producing more energy loss and reducing the device's CWR. Meanwhile, when the pitch motion response of the device reaches the maximum at $\omega = \omega_n$, there must be a change in α , and there should be a variation in electrical generation, which is unfavorable for the extraction of wave energy by the device.

Although S-TENGs based self-powered buoy is still in the research stage, its feasibility has been confirmed in a previous study that the self-powered buoy could light up a 12 W high-brightness LED light under wave action [19]. In practical engineering, the power range of some marine sensing facilities is 0.01–10 W, such as wave gauge ~ 0.02 W, pressure sensor ~ 0.7 W, oxygen sensor ~ 1.4 W, ultrasonic thickness gauge ~ 4.5 W [32]. Meanwhile, comparing the working conditions of WECs based on TENGs and EMGs (as shown in Table 7), TENGs can compensate for EMGs' inability to extract energy in low energy density seas. Therefore, S-TENGs based self-powered buoy is a competitive method to power offshore sensing facilities in low energy density seas.

In future work, two aspects can be considered to increase the self-powered buoy power output performances. With latching control, model predictive control, and multi-freedom combinations, the capture width of the device can be further enhanced [36–38]. On the other hand, the device's electrical output can be improved by adding management circuits, and treating the electrode surface [39,40].

4. Conclusions

The present study has developed a numerical model of S-TENG based self-powered buoy using the three-dimensional potential flow theory by the boundary element method. Subsequently, the model has been calibrated and verified by experiments. The hydrodynamic and electrical performances of the buoy under small-amplitude waves of centimeters high have been investigated using the model through numerical simulations and experiments. This investigation has found the following under the specific conditions of the present study:

- (1) The use of mechanical features of the PTFE balls motion in the S-TENG unit enables the PTO system to be simulated by a linear damping model in the pitch direction. The numerical results agree well with the experimental test, validating the availability of the numerical model of the self-powered buoy.
- (2) If the mooring chains are perpendicular to the wave ray, the device's movement amplitude can be increased whilst maintaining the power output stability.
- (3) Near the device's resonant frequency (ω_n), the capture width ratio of the device decreases significantly with increasing wave height from 4 cm to 6 cm.
- (4) The stability of the electrical output of the device reduces as the angle between the wave and the electrode direction changes within $(0.87-1.20)\omega_n$.
- (5) The capture width ratio of the self-powered buoy is 0.32, and the peak power of the device is 61.20 mW at $H_i = 6$ cm and $\omega = \omega_n$.

Overall, this study has analyzed the effects of mooring configurations, incident wave height, and wave frequency on the hydrodynamic and electrical performance of S-TENGs based self-powered buoy through numerical simulations and experiments. It has provided a reference for further optimization of the self-powered buoy. Moreover, it has offered the possibility of applying self-powered buoys based on TENGs to power sensing facilities such as lake aquaculture, marine ranching, and marine environmental monitoring.

Table 7

Working conditions comparison of WECs based on EMGs and TENGs.

| Mode | Classification | Wave Height (m) | Reference |
|-------|--------------------------|-----------------------------|---------------------------|
| EMGs | Point absorber | $1.0 \leq H_s \leq 6.5$ | Carballo et al. [33] |
| | Oscillating water column | $0.5 \leq H_s \leq 5.5$ | Veigas and Iglesias. [34] |
| | Point absorber | $1.0 \leq H_s \leq 8.0$ | Rusu and Onea [35] |
| | Overtopping converter | $1.0 \leq H_s \leq 8.0$ | Carballo et al. [33] |
| TENGs | Point absorber | $0.0625 \leq H_i \leq 0.25$ | Rodrigues et al. [15] |
| | Point absorber | $0.04 \leq H_i \leq 0.06$ | Present study |

H_s is the significant wave height, H_i is the incident wave height.

CRediT authorship contribution statement

Yunpeng Zhao: Conceptualization, Methodology, Resources, Supervision, Funding acquisition, Writing – review & editing. **Zhongqi Fan:** Conceptualization, Methodology, Software, Writing – original draft. **Chunwei Bi:** Methodology, Formal analysis, Supervision. **Hao Wang:** Methodology, Investigation. **Jianchun Mi:** Writing – review & editing. **Minyi Xu:** Funding acquisition, Conceptualization, Supervision.

Declaration of Competing Interest

The authors declare that they have no known competing financial interests or personal relationships that could have appeared to influence the work reported in this paper.

Acknowledgements

This work was financially supported by the National Key R&D Program of China (no. 2020YFE0200100); National Natural Science Foundation of China (nos. 51879022, 51979045, 52101400, 51822901, 31972843 and 31872610); LiaoNing Revitalization Talents Program (nos. XLYC907139 and XLYC2007045); Dalian Technology Talents Program, project no. 2020RQ107 and Program from Key Laboratory of Environment Controlled Aquaculture, Ministry of Education, China (no: 2021-MOEKLECA-KF-08). The Science and Technology Innovation 2025 Major Project of Ningbo, China, grant number 2020Z076.

References

- [1] Taveira-Pinto F, Iglesias G, Rosa-Santos P, Deng ZD. Preface to special topic: marine renewable energy. *J Renew Sustain Ener* 2015;7(6):061601. <https://doi.org/10.1063/1.4939086>.
- [2] Mustapa MA, Yaakob OB, Ahmed YM, Rheem C-K, Koh KK, Adnan FA. Wave energy device and breakwater integration: a review. *Renew Sustain Energy Rev* 2017;77:43–58.
- [3] Wu Z, Guo H, Ding W, Wang Y-C, Zhang L, Wang ZL. A hybridized triboelectric-electromagnetic water wave energy harvester based on a magnetic sphere. *ACS Nano* 2019. <https://doi.org/10.1021/acsnano.8b09088>.
- [4] Falcão AfD. Wave energy utilization: a review of the technologies. *Renew Sustain Energy Rev* 2010;14(3):899–918.
- [5] Lavidas G, Agarwal A, Venugopal V. Availability and accessibility for offshore operations in the mediterranean sea. *J Waterw Port Coastal Ocean Eng* 2018;144(6):05018006. [https://doi.org/10.1061/\(ASCE\)WW.1943-5460.0000467](https://doi.org/10.1061/(ASCE)WW.1943-5460.0000467).
- [6] Choupin O, Pinheiro Andutta F, Etemad-Shahidi A, Tomlinson R. A decision-making process for wave energy converter and location pairing. *Renew Sustain Energy Rev* 2021;147:111225. <https://doi.org/10.1016/j.rser.2021.111225>.
- [7] Kamranzad B, Hadadpour S. A multi-criteria approach for selection of wave energy converter/location. *Energy* 2020;204:117924. <https://doi.org/10.1016/j.energy.2020.117924>.
- [8] Fan F-R, Tian Z-Q, Lin Wang Z. Flexible triboelectric generator. *Nano Energy* 2012;1(2):328–34.
- [9] Wang Y, Liu X, Chen T, Wang H, Zhu C, Yu H, et al. An underwater flag-like triboelectric nanogenerator for harvesting ocean current energy under extremely low velocity condition. *Nano Energy* 2021;90:106503. <https://doi.org/10.1016/j.nanoen.2021.106503>.
- [10] Wang Y, Yang En, Chen T, Wang J, Hu Z, Mi J, et al. A novel humidity resisting and wind direction adapting flag-type triboelectric nanogenerator for wind energy harvesting and speed sensing. *Nano Energy* 2020;78:105279. <https://doi.org/10.1016/j.nanoen.2020.105279>.

- [11] Liu G, Guo H, Xu S, Hu C, Wang ZL. Oblate spheroidal triboelectric nanogenerator for all-weather blue energy harvesting. *Adv Energy Mater* 2019;1900801. <https://doi.org/10.1002/aenm.201900801>.
- [12] Yang J, Chen J, Liu Y, Yang W, Su Y, Wang ZL. Triboelectrification-based organic film nanogenerator for acoustic energy harvesting and self-powered active acoustic sensing. *ACS Nano* 2014;8(3):2649–57.
- [13] Zhang B, Wu Z, Lin Z, Guo H, Chun F, Yang W, et al. All-in-one 3D acceleration sensor based on coded liquid–metal triboelectric nanogenerator for vehicle restraint system. *Mater Today* 2021;43:37–44.
- [14] Mariello M, Guido F, Mastronardi VM, Todaro MT, Desmaële D, De Vittorio M. Nanogenerators for harvesting mechanical energy conveyed by liquids. *Nano Energy* 2019;57:141–56.
- [15] Rodrigues C, Ramos M, Esteves R, Correia J, Clemente D, Gonçalves F, et al. Integrated study of triboelectric nanogenerator for ocean wave energy harvesting: performance assessment in realistic sea conditions. *Nano Energy* 2021;84:105890. <https://doi.org/10.1016/j.nanoen.2021.105890>.
- [16] Zhang SL, Xu M, Zhang C, Wang Y-C, Zou H, He Xu, et al. Rationally designed sea snake structure based triboelectric nanogenerators for effectively and efficiently harvesting ocean wave energy with minimized water screening effect. *Nano Energy* 2018;48:421–9.
- [17] Xu M, Zhao T, Wang C, Zhang SL, Li Z, Pan X, et al. High power density tower-like triboelectric nanogenerator for harvesting arbitrary directional water wave energy. *ACS Nano* 2019. <https://doi.org/10.1021/acsnano.8b08274>.
- [18] Zhang X, Yu M, Ma Z, Ouyang H, Zou Y, Zhang SL, et al. Self-powered distributed water level sensors based on liquid-solid triboelectric nanogenerators for ship draft detecting. *Adv Funct Mater* 2019;29(41):1900327. <https://doi.org/10.1002/adfm.201900327>.
- [19] Wang H, Fan Z, Zhao T, Dong J, Wang S, Wang Y, et al. Sandwich-like triboelectric nanogenerators integrated self-powered buoy for navigation safety. *Nano Energy* 2021;84:105920. <https://doi.org/10.1016/j.nanoen.2021.105920>.
- [20] He F, Huang Z. Hydrodynamic performance of pile-supported OWC-type structures as breakwaters: an experimental study. *Ocean Eng* 2014;88:618–26.
- [21] Bachynski EE, Young YL, Yeung RW. Analysis and optimization of a tethered wave energy converter in irregular waves. *Renew Energy* 2012;48:133–45.
- [22] Canonsburg, PA, USA: ANSYS, Ltd; 2017.
- [23] Ogilvie TF. Recent progress towards the understanding and prediction of ship motions. Sixth symposium on naval hydrodynamics. *Onr Symp on Naval Hydrodynamics*; 1964.
- [24] Bearman PW, Downie MJ, Graham JM, Obasaju ED. Forces on cylinders in viscous oscillatory flow at low Keulegan-Carpenter numbers. *J Fluid Mech* 1985.
- [25] Chakrabarti SK. Offshore structure modeling: offshore structure modeling. *World Scientific* 1994.
- [26] Jung KH, Chang K-A, Jo HJ. Viscous effect on the roll motion of a rectangular structure. *J Eng Mech* 2006;132(2):190–200.
- [27] Chen HC, Liu T, Chang KA, Huang ET. Time-domain simulation of barge capsizing by a chimera domain decomposition approach. *International offshore and polar engineering conference; ISOPE-2002*. 2002.
- [28] Falnes J, Perlin M. Ocean waves and oscillating systems: linear interactions including wave-energy extraction. *Appl Mech Rev* 2003;56:286.
- [29] Tom N, Yeung RW. Performance enhancements and validations of the UC-Berkeley ocean-wave energy extractor. In: *ASME 2012 31st international conference on ocean, offshore and arctic engineering*; 2012.
- [30] Wang L, Isberg J, Tedeschi E. Review of control strategies for wave energy conversion systems and their validation: the wave-to-wire approach. *Renew Sustain Energy Rev* 2018;81:366–79.
- [31] Dong J, Wang H, Xiao X, Du T, Zhao Y, Fan Z, et al. Stackable triboelectric nanogenerators for self-powered marine monitoring buoy**. In: *2021 IEEE 16th international conference on nano/micro engineered and molecular systems (NEMS)*; 2021. p. 660–4.
- [32] Zhao T, Xu M, Xiao X, Ma Y, Li Z, Wang ZL. Recent progress in blue energy harvesting for powering distributed sensors in ocean. *Nano Energy* 2021;88:106199. <https://doi.org/10.1016/j.nanoen.2021.106199>.
- [33] Carballo R, Sánchez M, Ramos V, Taveira-Pinto F, Iglesias G. A high resolution geospatial database for wave energy exploitation. *Energy* 2014;68:572–83.
- [34] Veigas M, Iglesias G. Potentials of a hybrid offshore farm for the island of Fuerteventura. *Energy Convers Manage* 2014;86:300–8.
- [35] Rusu E, Onea F. Study on the influence of the distance to shore for a wave energy farm operating in the central part of the Portuguese nearshore. *Energy Convers Manage* 2016;114:209–23.
- [36] Shi H, Huang S, Cao F. Hydrodynamic performance and power absorption of a multi-freedom buoy wave energy device. *Ocean Eng* 2019;172:541–9.
- [37] Hals J, Falnes J, Moan T. A comparison of selected strategies for adaptive control of wave energy converters. *J Offshore Mech Arct Eng* 2011;133.
- [38] Hals J, Falnes J, Moan T. Constrained optimal control of a heaving buoy wave-energy converter. *J Offshore Mech Arct Eng* 2011;133.
- [39] Wang F, Tian J, Ding Y, Shi Y, Tao X, Wang X, et al. A universal managing circuit with stabilized voltage for maintaining safe operation of self-powered electronics system. *iScience* 2021;24(5):102502. <https://doi.org/10.1016/j.isci.2021.102502>.
- [40] Tang W, Jiang T, Fan FR, Yu AF, Zhang C, Cao X, et al. Liquid-metal electrode for high-performance triboelectric nanogenerator at an instantaneous energy conversion efficiency of 70.6%. *Adv Funct Mater* 2015;25(24):3718–25.